

Competing electronic orders on Kagome lattices at van Hove filling

Wan-Sheng Wang,¹ Zheng-Zhao Li,¹ Yuan-Yuan Xiang,¹ and Qiang-Hua Wang¹

¹*National Lab of Solid State Microstructures, Nanjing University, Nanjing, 210093, China*

The electronic orders in Hubbard models on a Kagome lattice at van Hove filling are of intense current interest and debate. We study this issue using the singular-mode functional renormalization group theory. We discover a rich variety of electronic instabilities under short range interactions. With increasing on-site repulsion U , the system develops successively ferromagnetism, intra-unit-cell antiferromagnetism, and charge bond order. With nearest-neighbor Coulomb interaction V alone ($U = 0$), the system develops intra-unit-cell charge density wave order for small V , s -wave superconductivity for moderate V , and the charge density wave order appears again for even larger V . With both U and V , we also find spin bond order and chiral $d_{x^2-y^2} + id_{xy}$ superconductivity in some particular regimes of the phase diagram. We find that the s -wave superconductivity is a result of charge density wave fluctuations and the squared logarithmic divergence in the pairing susceptibility. On the other hand, the d -wave superconductivity follows from bond order fluctuations that avoid the matrix element effect. The phase diagram is vastly different from that in honeycomb lattices because of the geometrical frustration in the Kagome lattice.

PACS numbers: 71.27.+a, 71.10.-w, 64.60.ae, 75.30.Fv

I. INTRODUCTION

The Kagome lattice model has attracted considerable attention duo to its high degree of geometrical frustration. In the Mott insulating limit, several possible states have been proposed as the ground state of the Heisenberg model in this lattice, such as the $U(1)$ algebraic spin liquid (SL),¹ the valance bond solid,² the triplet-gapped SL,³ and the singlet-gapped SL with signatures of Z_2 topological order.⁴ On the other hand, several exotic phases have been proposed for the Kagome Hubbard model, such as the ferromagnetism at electron filling $1/3$ (or $5/3$) per site,⁵ the fractional charge at $1/3$ filling for spinless fermions,⁶ and the Mott transition in anisotropic Kagome lattices.^{7,8}

Of particular interest is the possible phases at the van Hove filling (the filling fraction is $2/3 \pm 1/6$ per site), where the Fermi surface (FS) is perfectly nested and has saddle points on the edges of the Brillouine zone. These properties of the normal state makes it unstable against infinitesimal interactions. Similar FS appears in triangle and honeycomb lattices and were shown to develop, under short range repulsive interactions, chiral spin-density-wave (SDW) state⁹⁻¹¹ or chiral $d_{x^2-y^2} + id_{xy}$ superconducting state.^{12,13} Both states break time-reversal and parity symmetries, and are topologically nontrivial. Given the similar FS, a simple FS nesting argument would predict similar phases in the Kagome model. This seems to be the case in a recent variational cluster perturbation theory (with an additional spin disordered phase).¹⁴ However, as already realized in¹⁴ and emphasized in¹⁵, the interaction vertex viewed in the band basis has a strong momentum dependence (matrix element effect). This is because the character of the Bloch state on the FS depends on the position of the momentum. The matrix element effect weakens the nesting effect significantly for a local interaction U , leading to a new phase diagram in a recent analytical renormaliza-

tion group study.¹⁵ Such an analysis would be exact for a featureless fermi surface and infinitesimal interactions, but its applicability to the case of finite interactions together with perfect fermi surface nesting with van Hove singularity is an interesting issue to be addressed.

The functional renormalization group (FRG) method is a differential perturbation theory with respect to the increment of the phase space rather than in the interaction itself. It provides the flow of one-particle irreducible vertex functions versus the running parameter that controls the phase space.¹⁶ If implemented exactly the applicability of FRG is not limited by the size of the interaction. In practice, however, the vertices are truncated up to the four-point vertices under the assumption that higher order vertices are irrelevant. The FRG is promising to address finite interactions and treat particle-particle and particle-hole channels on equal footing. The applicability of FRG has been demonstrated in the contexts of cuprates¹⁷ and iron based superconductors.¹⁸ Recently, a singular-mode functional renormalization group (SMFRG) method was developed and applied to investigate topological superconductivity in correlated electron systems with or near van Hove singularities.^{11,19}

In this paper we perform SMFRG study of the model at van Hove filling. We discover a rich variety of electronic instabilities under short range interactions. With increasing on-site repulsion U , the system develops successively ferromagnetism (FM), intra unit-cell antiferromagnetism (AFM), and charge bond order (CBO). With nearest-neighbor Coulomb interaction V alone ($U = 0$), the system develops intra-unit-cell charge density wave (CDW) order for small V , s -wave superconductivity (s SC) for moderate V , and CDW appears again for even larger V . With both U and V , we also find spin bond order (SBO) and chiral $d_{x^2-y^2} + id_{xy}$ superconductivity (d SC). Our results are summarized in the phase diagram Fig.9. We find that the s SC is a result of CDW fluc-

tuations and the squared logarithmic divergence in the pairing susceptibility. On the other hand, the d SC follows from bond order fluctuations that avoid the matrix element effect. The phase diagram is vastly different from that in honeycomb lattices.

The rest of the paper is arranged as follows. In Sec. II, we define the model and illustrate the matrix element effect. In Sec. III, we introduce the FRG method. In Sec. IV, we first discuss the leading instabilities at typical points in the parameter space, and conclude by a discussion of the phase diagram. Finally, Sec. V is a summary and perspective of this work.

II. THE MODEL AND THE MATRIX ELEMENT EFFECT

The Hubbard model we used for the Kagome lattice is given by

$$H = -t \sum_{\langle ij \rangle \sigma} (c_{i\sigma}^\dagger c_{j\sigma} + \text{h.c.}) - \mu N_e + U \sum_i n_{i\uparrow} n_{i\downarrow} + V \sum_{\langle ij \rangle} n_i n_j, \quad (1)$$

where t is the hopping integral, $\langle ij \rangle$ denotes bonds connecting nearest-neighbor sites i and j , σ is the spin polarity, μ is the chemical potential, N_e is the total electron number operator, U is the on-site Hubbard interaction and V is the Coulomb interaction on nearest-neighbor bonds. Fig. 1(a) shows the structure of the Kagome lattice. The different symbols denote the three sublattices, and \mathbf{a} and \mathbf{b} are the two principle translation vectors. Fig. 1(b) shows the band structure of the model along high symmetry cuts in the Brillouine zone. The lower two bands cross at the Dirac point. The highest band is a flat band. The dashed line highlights the van Hove singularity. Fig. 1(c) shows the normal state density of states. The three sharp peaks arise from the van Hove singularities in the lower two bands and the third flat band. Fig. 1(d) shows the FS and the character of the Bloch states thereon. The FS appears to be perfectly nested. However, the character changes along each segment. The end points of each segment are saddle points. They have pure but different sublattice characters. The characters are mixed within the segment as shown by the color scale.

Consider the local interaction U for the moment. Such an interaction causes scattering at any wave vector. The nested FS would favor scattering connected by the nesting vectors and would lead to antiferromagnetism in usual case. *However, since U preserves sublattice indices, the character variation along the FS causes significant momentum dependence if U is projected to the band basis*, a matrix element effect as emphasized in¹⁵. This effect hampers the scattering significantly. To have a better idea of this effect, we calculate the zero frequency bare spin susceptibility $\chi_0(\mathbf{q})$ for site-local spin densities,

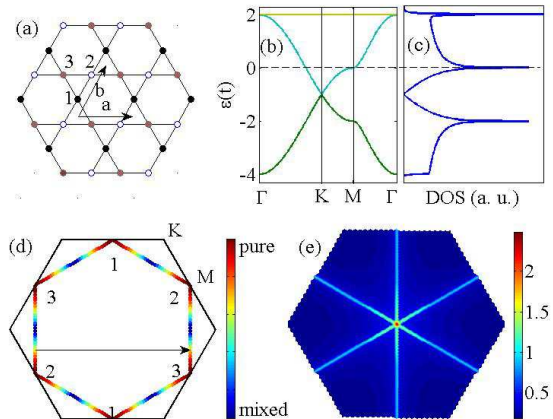


FIG. 1: (a) Structure of the Kagome lattice. Here $\mathbf{a} = (1, 0)$ and $\mathbf{b} = (1/2, \sqrt{3}/2)$ are the lattice unit vectors. The labels 1, 2, 3 denote the three sublattices. (b) The tight-binding dispersion along high symmetric directions. The dashed line is the Fermi level corresponding to the van Hove filling. (c) Normal state density of states. (d) Fermi surface and sublattice weights in the Bloch states thereon. On the endpoint of a fermi surface segment the Bloch state is contributed completely by one sublattice as indicated by the numbers. Within the segment the character are mixed as a superposition of the sublattice characters on the two endpoints. The arrow indicates one of the nesting vectors. (e) The largest eigenvalue of $\chi_0(\mathbf{q})$ as a function of \mathbf{q} .

where \mathbf{q} is the momentum transfer. The susceptibility is a matrix function in terms of the sublattice labels (α and β),

$$\chi_0^{\alpha\beta}(\mathbf{q}) = -\frac{T}{N} \sum_{\mathbf{k}, m} G^{\alpha\beta}(\mathbf{k}, i\omega_m) G^{\beta\alpha}(\mathbf{k} + \mathbf{q}, i\omega_m), \quad (2)$$

where T is the temperature, N the number of unit cells, \mathbf{k} the lattice momentum, ω_m the Matsubara frequency, and $G(\mathbf{k}, i\omega_m)$ the bare Green's function (in the sublattice basis). Fig. 1(e) shows the largest eigenvalue of $\chi_0(\mathbf{q})$ as a function of \mathbf{q} (for $T = 0.001t$). Instead of isolated peaks we see branch cuts of maxima in the momentum space. These cuts cross at the origin, where there is in fact a logarithmic singularity due to the saddle points. (The singularity is smeared by the finite size and finite temperature in the calculation). It is clear that site-local ferromagnetism rather than antiferromagnetism is the most favorable spin order, in contrast to the case in the honeycomb lattice.^{10,11} The lesson we learned from the above analysis is that for a multi-sublattice system the matrix element effect could weaken the nested scattering and alter the usual intuition regarding FS nesting. There is, however, a caveat in this kind of Stoner analysis, since it ignores mode-mode coupling between the particle-hole channels, and between particle-hole and particle-particle

channels. To treat all channels on equal footing we now switch to FRG.

III. THE SMFRG METHOD

In the following we apply a particular implementation of FRG, i.e., the SMFRG, which appears advantageous to treat systems with or near van Hove singularities.^{11,19,20} In this implementation, a generic four-point vertex function Γ_{1234} , which appears in the interaction $c_1^\dagger c_2^\dagger (-\Gamma_{1234}) c_3 c_4$, where $1 = (\mathbf{k}, \alpha)$ is a dummy label indicating the lattice momentum and sublattice label, is decomposed into the pairing (P), the crossing (C), and the direct (D) channels as

$$\begin{aligned} \Gamma_{\mathbf{k}+\mathbf{q},-\mathbf{k},-\mathbf{p},\mathbf{p}+\mathbf{q}}^{\alpha\beta\mu\nu} &\rightarrow \sum_{mn} f_m^*(\mathbf{k}, \alpha, \beta) P_{mn}(\mathbf{q}) f_n(\mathbf{p}, \nu, \mu), \\ \Gamma_{\mathbf{k}+\mathbf{q},\mathbf{p},\mathbf{k},\mathbf{p}+\mathbf{q}}^{\alpha\beta\mu\nu} &\rightarrow \sum_{mn} f_m^*(\mathbf{k}, \alpha, \mu) C_{mn}(\mathbf{q}) f_n(\mathbf{p}, \nu, \beta), \\ \Gamma_{\mathbf{k}+\mathbf{q},\mathbf{p},\mathbf{p}+\mathbf{q},\mathbf{k}}^{\alpha\beta\mu\nu} &\rightarrow \sum_{mn} f_m^*(\mathbf{k}, \alpha, \nu) D_{mn}(\mathbf{q}) f_n(\mathbf{p}, \mu, \beta). \end{aligned} \quad (3)$$

Here f_m is a set of orthonormal lattice form factors. A form factor defines a particular composite boson with definite collective momentum in the particle-hole or particle-particle channel, bearing a definite irreducible representation under the point group. The fact that the same generic vertex can be decomposed into different channels reflects the fact that these channels have mutual overlaps. The momentum space form factors are related to the real counterparts as, $f_m(\mathbf{k}, \alpha, \beta) = \sum_{\mathbf{r} \in m} f_m(\mathbf{r}, \alpha, \beta) e^{-i\mathbf{k}\cdot\mathbf{r}}$ where \mathbf{r} belongs to a set of bond vectors connecting sublattices α and β and assigned to m . In our practice the bond vectors are truncated up to those connecting the eighth neighbors (or third like-sublattice neighbors). In the following we use $m = (l, \alpha, \delta)$ to characterize the form factor label m , with l indicating the symmetry of the form factor, α one of the two sublattice labels, and δ a basis bond vector that can generate the set of bond vectors under the point group. This is applicable since we set the symmetry center at an atomic site so that the symmetry group is C_2 . Under this point group, α and β are invariant. There are only two irreducible representations A_g (even) and A_u (odd) for C_2 . We emphasize that even though the real-space range of the form factors is truncated the range of composite boson scattering is unlimited. This enables us to address the thermodynamic limit.

In the SMFRG, P , C and D are substituted into independent sets of one-loop and one-particle irreducible FRG Feynman diagrams where they would become potentially singular. (For example P is substituted into the particle-particle diagram.) This leads to the differential change ∂P , ∂C and ∂D with respect to the change of the running scale Λ , which we chose as the infrared cut-off of the Matsubara frequency. Since there are overlaps among the three channels, the full change is a sum of

the partial one plus the overlaps. It is in this sense that SMFRG takes care of mode-mode coupling and treats all channels on equal footing. This enables an initially repulsive pairing channel to become attractive at low energy scales, and is thus able to reflect the well-known Kohn-Luttinger anomaly.²¹ The technical details have been exposed elsewhere.^{11,22}

The effective interaction in the superconducting (SC), spin density wave (SDW), and CDW channels are given by $V_{sc} = -P$, $V_{sdw} = C$, and $V_{cdw} = C - 2D$, respectively. By singular value decomposition, we determine the leading instability in each channel,

$$V_x^{mn}(\mathbf{q}_x) = \sum_{\alpha} S_x^{\alpha} \phi_x^{\alpha}(m) \psi_x^{\alpha}(n), \quad (4)$$

where $x = sc, sdw, cdw$, S_x^{α} is the singular value of the α -th singular mode, ϕ_x^{α} and ψ_x^{α} are the right and left eigenvectors of V_x , respectively. We fix the phase of the eigenvectors by requiring $Re[\sum_m \phi_x^{\alpha}(m) \psi_x^{\alpha}(m)] > 0$ so that $S_x^{\alpha} < 0$ corresponds to an attractive mode in the x -channel. In the pairing channel $\mathbf{q}_{sc} = 0$ addresses the Cooper instability. The ordering wave vector in the SDW/CDW channel $\mathbf{q} = \mathbf{q}_{sdw/cdw}$ is chosen at which $V_{sdw/cdw}(\mathbf{q})$ has the most attractive eigenvalue. We note that such a vector has symmetry-related images, and may change during the FRG flow before settling down to fixed values. On the other hand, given the most singular mode, an effective field can be defined for the ordered state (or the condensed composite boson),

$$\begin{aligned} H_{sc} &= \sum_{m,\mathbf{k}} \psi_{sc}(m) f_m^*(\mathbf{k}, \alpha, \beta) c_{\mathbf{k},\alpha,\uparrow}^\dagger c_{-\mathbf{k},\beta,\downarrow}^\dagger + \text{h.c.}, \\ H_{cdw} &= \sum_{m,\sigma,\mathbf{k}} \psi_{cdw}(m) f_m^*(\mathbf{k}, \alpha, \beta) c_{\mathbf{k}+\mathbf{q}_{cdw},\alpha,\sigma}^\dagger c_{\mathbf{k},\beta,\sigma} + \text{h.c.}, \\ H_{sdw} &= \sum_{m,\mathbf{k}} \psi_{sdw}(m) f_m^*(\mathbf{k}, \alpha, \beta) c_{\mathbf{k}+\mathbf{q}_{sdw},\alpha,\uparrow}^\dagger c_{\mathbf{k},\beta,\downarrow} + \text{h.c.} \end{aligned} \quad (5)$$

up to global factors. It is understood that the sublattice labels α and β are determined by m according to our construction of form factors. The order parameters are encoded in the coefficients in the above field operators. Two remarks are in order. First there is a residual $SU(2)$ degeneracy in the case of triplet pairing and in the SDW order parameters. Second, the order parameters are in general nonlocal in real space (unless the contributing form factors are all local).

IV. SMFRG RESULTS

In this section we provide the SMFRG results for the model defined in the previous section. We begin by discussing the results at specific points in the parameter space (U, V) , and summarize the systematic results on a dense grid of (U, V) by a phase diagram.

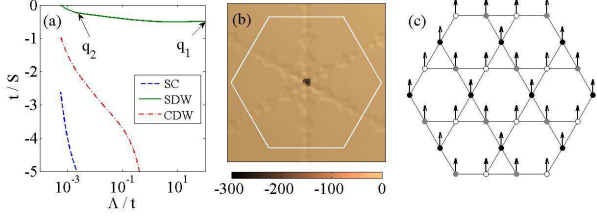


FIG. 2: (Color online) Results for $U = 2t$ and $V = 0$. (a) FRG flow of (the inverse of) the most singular values S in the SC (blue dashed line), SDW (green solid line), and CDW (red dashed-dot line) channels. (b) The renormalized interaction $\sum_m V_{sdw}^{mm}$ for $m = (A_g, \alpha, 0)$ ($\alpha = 1, 2, 3$) as a function of the collective momentum \mathbf{q} . The hexagon indicates the Brillouin-zone boundary. (c) The order parameter h_i (drawn as arrows) associated with the dominant SDW singular mode.

Ferromagnetic order: For $U = 2t$ and $V = 0$, Fig.2(a) shows the flow of the most negative singular values (denoted as S) in the SC, SDW, and CDW channels. Clearly the SDW (green solid line) is the leading instability. During the flow \mathbf{q}_{sdw} evolves from $\mathbf{q}_1 = (\pi, \pi/\sqrt{3})$ and settles down at $\mathbf{q}_2 = 0$. The renormalized interaction $\sum_m V_{sdw}^{mm}(\mathbf{q})$ for $m = (A_g, \alpha, 0)$ ($\alpha = 1, 2, 3$), which have dominant value in the leading singular mode, is shown in Fig.2(b). It has a strong peak at momentum $\mathbf{q} = 0$. Because the dominant form factor is local the ordered spin density is site-local. The effective field operator H_{sdw} according to Eq.(5) can be rewritten as $H_{sdw} = \sum_{i\sigma} h_i \sigma c_{i\sigma}^\dagger c_{i\sigma}$ with the order parameter h_i shown in Fig.2(c). This describes a FM order. The SC and CDW channel turn out to be sub-leading from Fig.2(a).

Intra-unit-cell antiferromagnetic order: For $U = 2.5t$ and $V = 0$, the flow of the singular values is shown in Fig.3(a). Again the SDW channel is the leading instability. During the flow, \mathbf{q}_{sdw} evolves from $\mathbf{q}_1 = (\pi, \pi/\sqrt{3})$ and settles down at $\mathbf{q}_2 = 0$, in the same fashion as above. Fig.3(b) shows the interaction $\sum_m V_{sdw}^{mm}(\mathbf{q})$ for $m = (A_g, \alpha, 0)$ ($\alpha = 1, 2, 3$). It also has a strong peak at momentum $\mathbf{q} = 0$. There are in fact two degenerate singular modes (apart from the SU(2) degeneracy). One of them leads to the order parameter h_i shown in Fig.3(c), with the ratio $0 : -1 : 1$ on the three sublattices. The other mode leads to a ratio $2 : -1 : -1$ (not shown). Both modes are antiferromagnetic within the unit cell, but are ferromagnetic from cell to cell. Comparing to the FM state, we call such a state the AFM state, although the ordering momentum is zero. A mean field analysis shows that in the ordered state the two degenerate modes are mixed in such a way that the spin pattern is as shown in Fig.3(d), with an angle of 120° between nearby spins. The SC and CDW channels remain to be sub-leading from Fig.3(a).

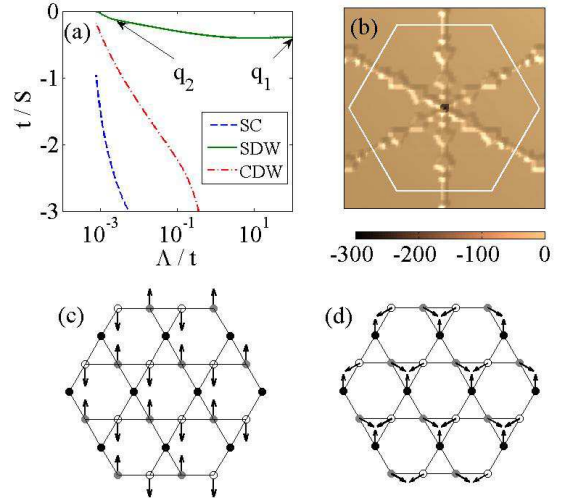


FIG. 3: (Color online) Results for $U = 2.5t$ and $V = 0$. (a) FRG flow of the most singular values in the SC (blue dashed line), SDW (green solid line), and CDW (red dashed-dot line) channels. (b) The renormalized interaction $\sum_m V_{sdw}^{mm}$ for $m = (A_g, \alpha, 0)$ ($\alpha = 1, 2, 3$) as a function of \mathbf{q} . (c) The order parameter h_i associated with one of the two degenerate SDW modes. (d) The spin structure in the mean field ordered state which combines the two degenerate singular modes.

Charge bond Order: From Fig.2 and Fig.3, we find that the CDW channel is enhanced with increasing U . This trend continues until the CDW channel becomes dominant for $U > 2.85t$. Fig.4(a) shows the FRG flow for $U = 3.5t$ and $V = 0$. During the flow the \mathbf{q}_{cdw} evolves but settles down at $\mathbf{q} = (0, 2\pi/\sqrt{3})$ (or its symmetric images) in the given view field. The dominant renormalized interaction $\sum_m V_{cdw}^{mm}(\mathbf{q})$, for $m = (A_u, 1, 1/4\hat{x} + \sqrt{3}/4\hat{y})$, $m = (A_u, 2, 1/2\hat{x})$ and $m = (A_u, 3, 1/4\hat{x} - \sqrt{3}/4\hat{y})$, is shown in Fig.4(b), where we see isolated peaks at the six nesting vectors (three of which are independent and correspond to the three form factors). We find that the effective field H_{cdw} constructed according to Eq.(5) for the above singular modes can be rewritten as $H_{cdw} = \sum_{\langle ij \rangle \sigma} \chi_{ij} (c_{i\sigma}^\dagger c_{j\sigma} + \text{h.c.})$, and is thus a CBO state. The pattern of the order parameter χ_{ij} depends on the ordering vector \mathbf{Q} . For $\mathbf{Q} = (0, 2\pi/\sqrt{3})$, it is shown in Fig.4(c). Notice that the field χ_{ij} is nonzero on parallel lines orthogonal to \mathbf{Q} . This is also the case for the other ordering momenta related to \mathbf{Q} by C_{6v} operations. Clearly, the CBO breaks both rotation and translation symmetries. The reason that the nesting vector is at work here is because the bond-centered charge density $\sum_{\sigma} (c_{i\sigma}^\dagger c_{j\sigma} + c_{j\sigma}^\dagger c_{i\sigma})$ connects different sublattices, and can take advantage of the inter-saddle scattering connected by the nesting vector. Notice that this kind of order is already beyond the mean field theory. It is a result of the overlap between the SDW and CDW channels as seen from Fig.4(a) where the

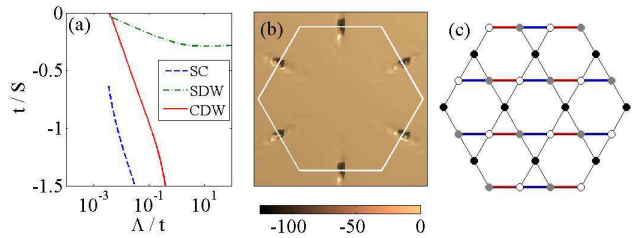


FIG. 4: (Color online) Results for $U = 3.5t$ and $V = 0$. (a) FRG flow of the most singular values S in the SC (blue dashed line), SDW (green dashed-dot line), and CDW (red solid line) channels. (b) The renormalized interaction $\sum_m V_{cdw}^{mm}$ for $m = (A_u, 1, 1/4\hat{x} + \sqrt{3}/4\hat{y})$, $m = (A_u, 2, 1/2\hat{x})$ and $m = (A_u, 3, 1/4\hat{x} - \sqrt{3}/4\hat{y})$, as a function of \mathbf{q} . The three independent peaks correspond to the three form factors, respectively. (c) The real space structure of the order parameter χ_{ij} associated with one of the dominant CDW modes with the ordering momentum $\mathbf{Q} = (0, 2\pi/\sqrt{3})$. The red (blue) color indicates χ_{ij} is positive (negative).

SDW channel dominates at high energy scales. The pairing channel is still subdominant here.

Intra-unit-cell Charge density wave: We now consider the effect of the nearest neighbor interaction V . Fig.5(a) shows the FRG flow for $U = 0$ and $V = 0.25t$. It is clear that the CDW channel (red solid line) is the leading instability. During the flow the \mathbf{q}_{cdw} evolves from $\mathbf{q}_1 = (0, 2/\sqrt{3})\pi$ to $\mathbf{q}_2 = (0, 0.385)\pi$ and finally settles down at $\mathbf{q}_3 = 0$. The dominant renormalized interaction $\sum_m V_{cdw}^{mm}$ for $m = (A_g, \alpha, 0)$ ($\alpha = 1, 2, 3$) shown in Fig.5(b) has a sharp peak at $\mathbf{q} = 0$. There are two degenerate singular modes. The effective field H_{cdw} constructed according to Eq.(5) can be rewritten as $H_{cdw} = \sum_{i\sigma} \eta_i c_{i\sigma}^\dagger c_{i\sigma}$ with the order parameter η_i shown in Fig.5(c) and (d) for the two singular modes. This is an intra-unit-cell CDW state. It breaks rotational symmetry but does not break the translation symmetry. It is therefore an analogue of the Pomeranchuk instability on square lattices.²³ The SDW and SC channels are sub-leading in this case.

S-wave superconductivity: The FRG flow for $U = 0$ and $V = 0.5t$ is shown in Fig.6(a). We find that the SC channel is the leading instability. Fig.6(b) shows the renormalized interaction V_{sc}^{mm} for $m = (A_g, 1, 0)$. (By symmetry, interactions involving form factors centered on the other sublattices contribute similarly.) Inspection of the eigenfunction ϕ_{sc} reveals that it has dominant values for A_g form factors involving $\mathbf{r} = 0$ and subdominant values for A_g form factors involving \mathbf{r} connecting nearest like-sublattice neighbors. The gap function from H_{sc} constructed according to Eq.(5) projected on the fermi surface is shown in Fig.6(c). Clearly it is an sSC gap function. Such a pairing symmetry

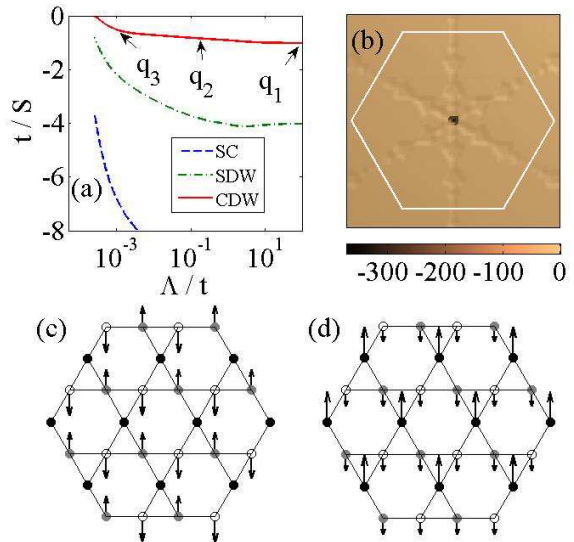


FIG. 5: (Color online) Results for $U = 0$ and $V = 0.25t$. (a) The FRG flow the most singular values S in the SC (blue dashed line), SDW (green dashed-dot line), and CDW (red solid line) channels. (b) The renormalized interaction $\sum_m V_{cdw}^{mm}$ for $m = (A_g, \alpha, 0)$ ($\alpha = 1, 2, 3$) as function a function of \mathbf{q} . (c) and (d) show the order parameter η_i associated with the two degenerate CDW singular modes. The length of the arrows indicate the amplitude and the direction of the arrow indicate the sign of the order parameter.

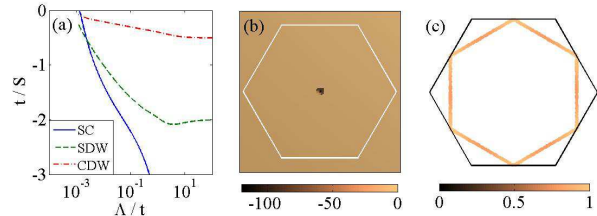


FIG. 6: (Color online) Results for $U = 0$ and $V = 0.5t$. (a) The FRG flow the most singular values S in the SC (blue solid line), SDW (green dashed-dot line), CDW (red dashed-dot line) channels. (b) The renormalized interaction $V_{sc}^{mm}(\mathbf{q})$ for $m = (A_g, 1, 0)$ as a function of \mathbf{q} . (c) The momentum space gap function on the Fermi surface associated with the SC singular mode.

persists for small $U > 0$. However the dominant pairing amplitude for $U = 0$ is on-site, while the amplitude on bonds (connecting nearest like-sublattices) increases and eventually dominates with increasing U . Inspection of Fig.6(a) reveals that such an s-wave pairing follows from the overlap with the CDW channel.

Spin bond order: The FRG flow for $U = V = 0.75t$ is shown in Fig.7(a). Clearly the SDW (green solid line) is the leading instability. During the flow \mathbf{q}_{sdw} evolves from $\mathbf{q}_1 = (0, 2/\sqrt{3})\pi$ to $\mathbf{q}_2 = 0$ and finally settles

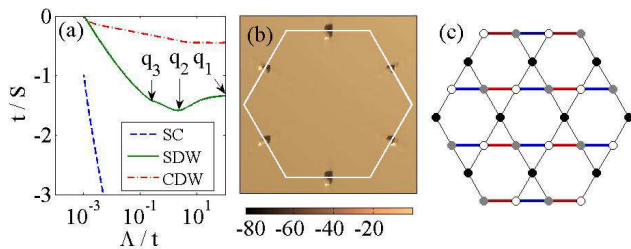


FIG. 7: (Color online) Results for $U = V = 0.75t$. (a) FRG flow of the most singular values S in the SC (blue dashed line), SDW (green solid line), and CDW (red dashed-dot line) channels. (b) The renormalized interaction $\sum_m V_{sdw}^{mm}$ for $m = (A_u, 1, 1/4\hat{x} + \sqrt{3}/4\hat{y})$, $m = (A_u, 2, 1/2\hat{x})$, and $m = (A_u, 3, 1/4\hat{x} - \sqrt{3}/4\hat{y})$ as a function of \mathbf{q} . The three independent peak momenta corresponds to the three form factors, respectively. (c) The real space structure of the order parameter ξ_{ij} associated with one of the SDW singular modes with the ordering momentum $\mathbf{Q} = (0, 2\pi/\sqrt{3})$. The blue (red) bond indicates that ξ_{ij} is positive (negative).

down at $\mathbf{q}_3 = \mathbf{q}_1$. Fig.7(b) shows the renormalized interaction $\sum_m V_{sdw}^{mm}$ for $m = (A_u, 1, 1/4\hat{x} + \sqrt{3}/4\hat{y})$, $m = (A_u, 2, 1/2\hat{x})$ and $m = (A_u, 3, 1/4\hat{x} - \sqrt{3}/4\hat{y})$, where we see isolated peaks at the six nesting vectors (three of which are independent and correspond to the three form factors). The effective field operator in the real space can be written as $H_{sdw} = \sum_{\langle ij \rangle \sigma} \xi_{ij} \sigma (c_{i\sigma}^\dagger c_{j\sigma} + c_{j\sigma}^\dagger c_{i\sigma})$ (apart from the SU(2) degeneracy). The pattern of the order parameter ξ_{ij} depends on the ordering vector \mathbf{Q} . For $\mathbf{Q} = (0, 2\pi/\sqrt{3})$, it is shown in Fig.7 (c). As in the case of CBO state, the order parameter ξ_{ij} is nonzero on parallel lines orthogonal to \mathbf{Q} . This describes an SBO state. The SC and CDW channel is sub-leading in this case.

Chiral $d_{x^2-y^2} + id_{xy}$ superconductivity. Fig.8(a) shows the FRG flow for $U = 2t$ and $V = 1.5t$. Clearly, the SC channel is the leading instability. Fig.8(b) shows the renormalized interaction V_{sc}^{mm} for $m = (A_g, 1, 1/2\hat{x} + \sqrt{3}/2\hat{y})$. Such a form factor shows the pairing is on third-neighbor bonds (or nearest like-sublattice neighbor bonds). From the singular mode ϕ_{sc} we construct the effective pairing operator H_{sc} , and get the gap function in the momentum space as shown in Fig.8(c). This is clearly a d_{xy} -wave gap function. In fact there is another degenerate singular mode which gives a $d_{x^2-y^2}$ -wave gap function (not shown). Using the renormalized pairing interaction we performed mean field calculations to find that the ordered state is a chiral $d_{x^2-y^2} + id_{xy}$ superconducting state, which we call the dSC state. The chiral state is fully gapped on the fermi surface and thus saves more energy. Fig.8(a) shows that the SDW and CDW channels are dominant at high energy scales. Inspection of the later stage of the FRG flow reveals that the singular modes in these channels contains dominant CBO and SBO components

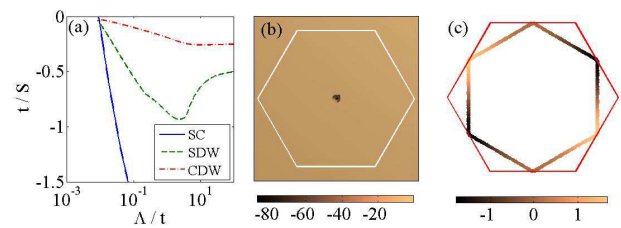


FIG. 8: (Color online) Results for $U = 2t$ and $V = 1.5t$. (a) FRG flow of the most singular values S in the SC (blue solid line), SDW (green dashed line), and CDW (red dashed-dot line) channels. (b) The renormalized interaction $V_{sc}^{mm}(\mathbf{q})$ for $m = (A_g, 1, 1/2\hat{x} + \sqrt{3}/2\hat{y})$ as a function of \mathbf{q} . (c) The momentum space gap function on the Fermi surface associated with one of the two degenerate SC singular modes.

(on nearest bonds). We shall come back to this point later.

The phase diagram: Apart from the typical results discussed above, we have performed systematic SMFRG calculations on a dense grid in the (U, V) plane. The results are summarized as a phase diagram shown in Fig.9. The CBO and SBO states have ordering momenta at one of the nesting vectors, while the others order at zero momentum without breaking translation symmetry. However, the CDW and AFM states have intra-unit-cell structures. This phase diagram can be understood as follows.

Along the $U = 0$ axis, the s -wave superconductivity appears inbetween the intra-unit-cell CDW states at small and large values of V . This is counter-intuitive at a first sight since increasing V would favor CDW further. However, the numerical result is reasonable for the following reasons. While the CDW susceptibility behaves as $\ln(W/\Lambda)$ at the running scale Λ because of the van Hove singularities in the normal state density of states (here W is of the order of the bandwidth), the SC susceptibility diverges as $\ln^2(W/\Lambda)$ due to a further Cooper instability.¹² Therefore, once the initially repulsive pairing channel becomes slightly attractive via the overlap with the CDW channel, the pairing interaction could grow in magnitude faster than the CDW interaction, and could eventually overwhelm the CDW interaction. This explains the emergence of the s -wave superconductivity for moderate V . However, if V is initially small, the overlap with the SC channel is small during the flow. On the other hand, if V is large enough, the CDW channel diverges before the SC channel takes advantage of the fast growth. These considerations are consistent with our results along the $U = 0$ axis.

In the phase diagram we see that both CBO and SBO phases are in proximity to the d -wave SC phase. This is a reasonable result since we find that the bond orders are on nearest-neighbor bonds, while the d -wave pairing are on third-neighbor bonds (or nearest like-sublattice neighbor bonds). It is the even order processes involv-

ing the bond-density interactions that have overlap with the above singlet pairing interaction, which are therefore immune to the sign structure in the SBO and CBO interactions. On the other hand, the on-site repulsion disfavors s -wave pairing. This makes d -wave pairing viable. Interestingly by utilizing the bond order fluctuations the pairing mechanism avoids the matrix element effect that would frustrate site-local spin fluctuations at the nesting vector.

Along the $V = 0$ axis, our SMFRG result predicts the charge bond order for large U . This is indeed a spin disordered phase as found in¹⁴, and is beyond the mean field theory but consistent with the lack of a well defined site-local spin ordered phase. The reason that a large U favors a spin disordered state rather than local spin moment ordering is twofold. First the matrix element effect weakens nested scattering and favors ferromagnetic ordering. Second a sufficiently large U makes the nested scattering more important as compared to the case of small U . This would favor antiferromagnetic ordering. The site-local spin ordering is thus frustrated by the competition of ferromagnetism and antiferromagnetism. The compromise is the CBO state, which is an analogue of the valence bond solid and reflects the short-range spin correlations. The limit of $U \gg t$ is beyond the scope of our SMFRG, but enables mapping of the model to a doped $t - J$ model. We leave it for further investigations.

Finally, for $U \sim t$ and with increasing V , the successive orders are FM, CBO, SBO, d SC, s SC and CDW. This sequence is reasonable as follows. The CBO and SBO states take advantage of V since by connecting different sublattices it avoids the matrix element effect. However, a large V favors CDW. In the intermediate region, the CBO/SBO fluctuations drive d SC while CDW fluctuations drives s SC, as discussed above. This explains why there is a transition from d SC to s SC with increasing V .

V. SUMMARY AND PERSPECTIVE

In summary, we have studied the extended Hubbard model on Kagome lattice at van Hove filling using the SMFRG method. We discovered a variety of phases in the parameter space. Along the $V = 0$ axis and with increasing on-site repulsion U , the system develops successively ferromagnetism, intra unit-cell antiferromagnetism, and charge bond order. With nearest-neighbor Coulomb interaction V alone ($U = 0$), the system develops intra-unit-cell charge density wave order for small V , s -wave superconductivity for moderate V , and CDW appears again for even larger V . With both U and V , we also find spin bond order and chiral $d_{x^2-y^2} + id_{xy}$ superconductivity. We find that the s -wave superconductivity is a result of CDW fluctuations and the squared logarithmic divergence in the pairing susceptibility. On the other hand, the d -wave

superconductivity follows from bond order fluctuations that avoid the matrix element effect. We summarized

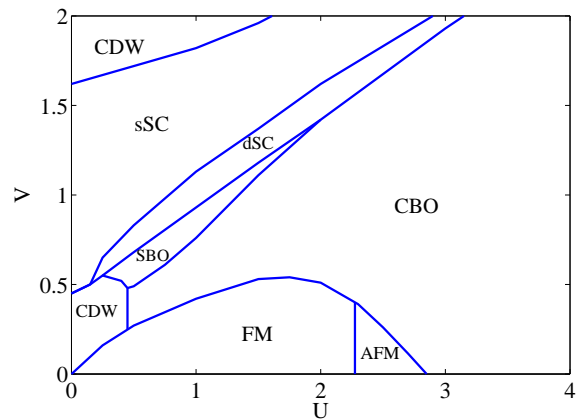


FIG. 9: The phase diagram of the Kagome lattice at van Hove filling. The electronic orders and the associated ordering momenta are: FM ($\mathbf{Q} = 0$), intra-unit-cell AFM ($\mathbf{Q} = 0$), CBO ($\mathbf{Q} = \mathbf{M}$), intra-unit-cell CDW ($\mathbf{Q} = 0$), SBO ($\mathbf{Q} = \mathbf{M}$), $d_{x^2-y^2} + id_{xy}$ -wave SC (d SC, $\mathbf{Q} = 0$) and s -wave SC (s SC, $\mathbf{Q} = 0$). Here \mathbf{M} is one of the nesting vectors connecting the saddle points on the fermi surface.

the results by the phase diagram in Fig.9. It is vastly different from that in honeycomb lattices, and the difference can be attributed to the frustrating matrix element effect.

We notice that the spin 1/2 Kagome lattice has been realized in Herbertsmithite $ZnCu_3(OH)_3Cl_2$ ^{24,25} and its isostructural Mg-based paracatamite $MgCu_3(OH)_6Cl_2$.²⁶ Also, the optical Kagome lattice has been simulated experimentally in ultra-cold atomic gases, and the optical wavelengths can be suitably adjusted for fermionic isotopes such as 6Li and 40K .²⁷ With the possibility of tuning U and V continuously, the optical lattice with ultracold atomic gases are most promising to realize the predictions presented in this paper.

During the writing of this paper we became aware of a parallel work in which a similar scenario is addressed.²⁸

Acknowledgments

QHW thanks Jian-Xin Li and Fan Yang for interesting discussions. The project was supported by NSFC (under grant No.10974086 and No.11023002) and the Ministry of Science and Technology of China (under grant No.2011CBA00108 and 2011CB922101).

-
- ¹ Y. Ran, M. Hermele, P. A. Lee, and X.-G. Wen, *Phys. Rev. Lett.* **98**, 117205 (2007).
- ² R. R. P. Singh and D. A. Huse, *Phys. Rev. B* **76**, 180407 (2007).
- ³ H. C. Jiang, Z. Y. Weng, and D. N. Sheng, *Phys. Rev. Lett.* **101**, 117203 (2008).
- ⁴ S. Yan, D. A. Huse, and S. R. White, *Science* **332**, 1173 (2011).
- ⁵ F. Pollmann, P. Fulde, and K. Shtengel, *Phys. Rev. Lett.* **100**, 136404 (2008).
- ⁶ A. O'Brien, F. Pollmann, P. Fulde, *Phys. Rev. B* **81**, 235115 (2010).
- ⁷ Y. Furukawa, T. Ohashi, Y. Koyama, and N. Kawakami, *Phys. Rev. B* **82**, 161101 (2010).
- ⁸ A. Yamada, K. Seki, R. Eder, and Y. Ohta, *Phys. Rev. B* **83**, 195127 (2011).
- ⁹ I. Martin and C. D. Batista, *Phys. Rev. Lett.* **101**, 156402 (2008).
- ¹⁰ Li Tao, *Eur. Phys. Lett.* **97**, 37001 (2012).
- ¹¹ W. S. Wang, Y. Y. Xiang, Q. H. Wang, F. Wang, F. Yang, and D. H. Lee, *Phys. Rev. B* **85**, 035414 (2012).
- ¹² R. Nandkishore, L. S. Levitov, and A. V. Chubukov, *Nat. Phys.* **8**, 158 (2012).
- ¹³ M. Kiesel, C. Platt, W. Hanke, D. A. Abanin, and R. Thomale, e-print arXiv:1109.2953.
- ¹⁴ S. L. Yu and J. X. Li, *Phys. Rev. B* **85**, 144402 (2012).
- ¹⁵ M. Kiesel and R. Thomale, e-print arXiv:1206.6539.
- ¹⁶ C. Wetterich, *Nucl. Phys. B*, **352**, 529 (1991).
- ¹⁷ C. Honerkamp, M. Salmhofer, N. Furukawa, and T. M. Rice, *Phys. Rev. B* **63**, 035109 (2001). M. Ossadnik, C. Honerkamp, T. M. Rice, and M. Sigrist, *Phys. Rev. Lett.* **101**, 256405 (2008). F. Wang, H. Zhai, and D. H. Lee, *Phys. Rev. B* **80**, 064517 (2009).
- ¹⁸ F. Wang, H. Zhai, Y. Ran, A. Vishwanath, and D.-H. Lee, *Phys. Rev. Lett.* **102**, 047005 (2009). R. Thomale, C. Platt, J. P. Hu, C. Honerkamp, and B. A. Bernevig, *Phys. Rev. B* **80**, 180505 (2009). F. Wang, H. Zhai, and D. H. Lee, *Phys. Rev. B* **81**, 184512 (2010). R. Thomale, C. Platt, W. Hanke, and B. A. Bernevig, *Phys. Rev. Lett.* **106**, 187003 (2011).
- ¹⁹ Y. Y. Xiang, W. S. Wang, Q. H. Wang and D. H. Lee, *Phys. Rev. B* **86**, 024523 (2012).
- ²⁰ C. Husemann and M. Salmhofer, *Phys. Rev. B* **79**, 195125 (2009).
- ²¹ W. Kohn and J. M. Luttinger, *Phys. Rev. Lett.* **15**, 524 (1965).
- ²² In order to see how the normal state becomes unstable it is a usual practice to ignore the flow of the two-point vertex, which is nothing but the inverse of one-particle Green's function. We also ignore the frequency dependence of the four-point vertices under the usual assumption that the frequency dependence is irrelevant.
- ²³ C. J. Halboth and W. Metzner, *Phys. Rev. Lett.* **85**, 5162 (2000).
- ²⁴ M. P. Shores, E. A. Nytko, B. M. Bartlett, and D. G. Nocera, *J. Am. Chem. Soc.* **127**, 13462 (2005).
- ²⁵ S. H. Lee, H. Kikuchi, Y. Qiu, B. Lake, Q. Huang, K. Habicht, and K. Kiefer, *Nat. Matter.* **6**, 853 (2007).
- ²⁶ E. Kermarrec, P. Mendels, F. Bert, R. H. Colman, A. S. Wills, P. Strobel, P. Bonville, A. Hillier, and A. Amato, *Phys. Rev. B* **84**, 100401 (2011).
- ²⁷ G. B. Jo, J. Guzman, C. K. Thomas, P. Hosur, A. Vishwanath, and D. M. Stamper-Kurn, *Phys. Rev. Lett.* **108**, 045305 (2012).
- ²⁸ R. Thomale, et al, unpublished.